Preprint
UCRL-JC-136906

Thermomechanical Characterization of Nickel-Titanium-Copper Shape Memory Alloy Films

K. P. Seward, P. B. Ramsey, P. Krulevitch

This article was submitted to
Symposium on Properties of Structural Films, Orlando, FL.,
November 15-16, 2000

U.S. Department of Energy

Lawrence
Livermore
National
Laboratory

October 31, 2000

Approved for public release; further dissemination unlimited

DISCLAIMER

This document was prepared as an account of work sponsored by an agency of the United States Government. Neither the United States Government nor the University of California nor any of their employees, makes any warranty, express or implied, or assumes any legal liability or responsibility for the accuracy, completeness, or usefulness of any information, apparatus, product, or process disclosed, or represents that its use would not infringe privately owned rights. Reference herein to any specific commercial product, process, or service by trade name, trademark, manufacturer, or otherwise, does not necessarily constitute or imply its endorsement, recommendation, or favoring by the United States Government or the University of California. The views and opinions of authors expressed herein do not necessarily state or reflect those of the United States Government or the University of California, and shall not be used for advertising or product endorsement purposes.

This is a preprint of a paper intended for publication in a journal or proceedings. Since changes may be made before publication, this preprint is made available with the understanding that it will not be cited or reproduced without the permission of the author.

This work was performed under the auspices of the United States Department of Energy by the University of California, Lawrence Livermore National Laboratory under contract No. W-7405-Eng-48.

This report has been reproduced directly from the best available copy.

Available electronically at http://www.doc.gov/bridge

Available for a processing fee to U.S. Department of Energy
And its contractors in paper from
U.S. Department of Energy
Office of Scientific and Technical Information
P.O. Box 62
Oak Ridge, TN 37831-0062
Telephone: (865) 576-8401
Facsimile: (865) 576-5728
E-mail: reports@adonis.osti.gov

Available for the sale to the public from
U.S. Department of Commerce
National Technical Information Service
5285 Port Royal Road
Springfield, VA 22161
Telephone: (800) 553-6847
Facsimile: (703) 605-6900
E-mail: orders@ntis.fedworld.gov
Online ordering: http://www.ntis.gov/ordering.htm

OR

Lawrence Livermore National Laboratory
Technical Information Department's Digital Library
http://www.llnl.gov/tid/Library.html

Kirk P. Seward,[1] Philip B. Ramsey,[1] and Peter Krulevitch,[1]

Thermomechanical Characterization of Nickel-Titanium-Copper Shape Memory Alloy Films

REFERENCE: Seward, K. P., Ramsey, P. B. and Krulevitch, P., "Thermomechanical Characterization of Nickel-Titanium-Copper Shape Memory Alloy Films," *Mechanical Properties of Structural Films, STP 1413*, C. Muhlstein and S. Brown, Eds., American Society for Testing and Materials, West Conshohocken, PA, 2000.

ABSTRACT: In an effort to develop a more extensive model for the thermomechanical behavior of shape memory alloy (SMA) films, a novel characterization method has been developed. This automated test has been tailored to characterize films for use in micro-electromechanical system (MEMS) actuators. The shape memory effect in NiTiCu is seen in the solid-state phase transformation from an easily deformable low-temperature state to a "shape remembering" high-temperature state. The accurate determination of engineering properties for these films necessitates measurements of both stress and strain in microfabricated test structures over the full range of desired deformation. Our various experimental methods (uniaxial tensile tests, bimorph curvature tests and diaphragm bulge tests) provide recoverable stress and strain data and the stress-strain relations for these films. Tests were performed over a range of temperatures by resistive heating or ambient heating. These measurements provide the results necessary for developing active SMA structural film design models.

KEYWORDS: Shape memory, NiTiCu, nickel-titanium-copper, Nitinol, NiTi, TiNi, MEMS, microactuators.

Introduction

The use of active materials actuation systems in micro-electromechanical systems (MEMS) is becoming more popular as solutions are sought for providing effective motion and force control on the microscale. Shape memory alloy films are an attractive solution in these systems because they provide the highest work output per unit volume of any microactuator alternatives (seen in Fig. 1) [*1*]. Concepts exist to use shape memory alloys (SMAs) in microvalves, pumps and actuators [*2-4*], and several scientists [1,5-7] have characterized individual characteristics of SMAs. The tests and results described here move us one step closer to a comprehensive SMA characterization tool to allow effective and optimal design of MEMS that fully utilize actuation properties.

Performing a comprehensive engineering analysis of this material has relied on the

[1] Lawrence Livermore National Laboratory, PO Box 808, L-223, Livermore, CA 94550. Phone (925) 424-5218. Email kirkpatrick@alum.mit.edu

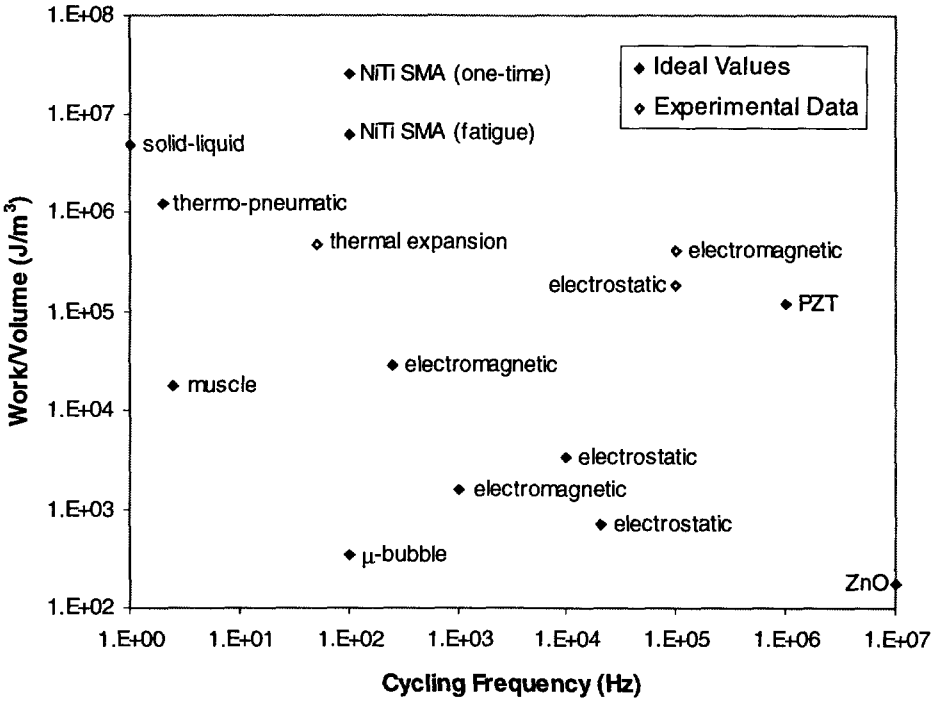

FIG. 1—*Work output per unit volume vs. operating frequency for several standard microactuators.*

design of MEMS devices with incorporated SMA films. Microfabrication methods were used to generate test chips with the goals of avoiding alloy recrystallization and creating devices with similar geometry and scale to actual MEMS actuators that would operate via a shape memory effect. The testing method used here provides data based on the resistive heating of the films rather than ambient heating. Alloy characterization has been performed by other researchers to derive stress-strain relationships under isothermal conditions or with temperature as a monitored variable [*1,5-7*]. Alternatively, this test utilizes resistive heating and thus constant current conditions are imposed on the films in a room temperature environment. Varying the strain and measuring the stress on the films under these conditions allows the plotting of characteristic curves and the derivation of constitutive relations for use in the design of new actuators.

Because SMA films behave differently than bulk materials and vary in mechanical properties with distinct fabrication methods, a simple technique to provide all necessary mechanical data is beneficial. The automated test described here is non-destructive and provides a comprehensive range of thermomechanical and electromechanical information with simultaneous determination of stress-strain behavior and material resistivity of both phases, recoverable stress and strain against a load, actuation fatigue behavior, response and cycling times, and power requirements for actuation of fixed-fixed NiTiCu ribbons.

This paper begins by addressing the theory behind the shape memory effect. While a thorough knowledge of the phase transformations that allow shape memory are not entirely necessary to design actuators, an understanding of the materials science certainly aids in the design process. The fabrication of test structures used for these tests is

described, with a list of processes that are not detrimental to shape memory film integrity. The testing methods are discussed along with the characteristic equations that allow formation of stress and strain relationships. Finally, results are presented based on our findings during uniaxial tensile tests, bimorph curvature tests, and diaphragm bulge tests.

Shape Memory Theory

Shape memory alloys are appropriately named because they "remember" their shape while undergoing a solid-to-solid phase transformation during heating. At room temperature, NiTiCu is in its low-temperature, martensite state. When it is heated beyond its transformation temperature, it undergoes the phase transformation to an austenite state. In the martensite phase, the material exhibits higher ductility than the austenite phase and is therefore easily deformed. When the material is heated it enters the austenite phase (known as reverse transformation). It regains its original shape as long as permanent plastic deformation did not occur in the martensite phase (around 4-10% strain for most SMA's [*8*]). Upon cooling to martensite again (martensite transformation), the SMA does not change macroscopic shape unless external loads are applied. In the two-way shape memory effect, both phases remember a unique shape [*9-10*], which can occur due to residual film stresses changing the shape of the material during the austenite to martensite transformation in the absence of external loading. Electrical resistance changes from the martensite phase to the austenite phase have been observed by other researchers [*7,11-12*] and were also studied in these experiments.

Shape memory transformations occur by solid-to-solid phase transitions from one crystal lattice structure to another, sometimes with an intermediate phase during heating or cooling. In NiTi, the austenite phase, or parent phase, has a tightly packed B2 structure, with the same symmetry as the body centered cubic lattice but with alternating atoms. The martensite phase is monoclinic or orthorhombic subject to alloy composition. NiTi martensite is monoclinic and NiTiCu martensite is orthorhombic. During the NiTi phase transformation upon cooling from austenite to martensite, the alloy passes through its intermediate R-phase, which has been described as both rhombohedral and orthorhombic by different scientists [*13-15*]. As the Cu content increases (substituting for nickel) from zero to 10% by weight, the alloy experiences phase transitions upon cooling of B2 $\rightarrow$ monoclinic, B2 $\rightarrow$ orthorhombic $\rightarrow$ monoclinic, and finally B2 $\rightarrow$ orthorhombic lattice structure [*15*]. The addition of Cu to NiTi acts to stabilize the dependence between transformation temperatures and alloy composition. It also leads to smaller hysteresis in the alloy's transformation temperatures [*16*].

Martensite Phase

The martensite phase has been described as ductile in its deformation. The reason behind this is the twinned structure encountered in martensite. For MEMS applications, the twinning dimensions are on the order of nanometers while the material dimensions are on the order of microns. This highly twinned structure is ductile because twin planes are able to slip with respect to one another. Since twins are moving with respect to each other, dislocations do not appear and there is no permanent, irrecoverable deformation. This leads to the method of interpreting the presence of twins in NiTi based shape memory alloys, as reported by Bhattacharya [*17*]:

1. The lattice on one side can be obtained by a simple shear of the lattice on the other.

2. The lattice on one side can also be obtained by a rotation of the lattice on the other.

These conditions are at the heart of twin variants. When lattices are sheared or rotated, they transform from one variant of the martensitic lattice structure into another. Thus, variants change because of the twinned microstructure, which appears as macroscopic plastic deformation. The kinematic compatibility of the material states that the deformation of the material must be coherent, so macroscale martensitic material appears to have the same properties throughout, though it is made up of several variants of one lattice structure [*17*].

Martensitic material takes on the material property known as self-accommodation. This property allows for no macroscopic change in shape in the absence of external loads when the material transforms from austenite to martensite. During phase transformation, the new martensite variants align themselves to allow no macroscopic shape change in the material. Cooling the material below its transformation temperature can form the ductile martensite microstructure, but martensite can also be formed by physically increasing the transformation temperature. This behavior, known as stress-induced twinning, is governed by the Clausius-Clapeyron relationship, which states that as the stress and strain in the material increase, the martensite transformation temperature also increases. The balance between strain energy and heat energy therefore dictate whether the alloy is acting as a ductile martensite or a stiff austenite [*18*].

Austenite Phase

Since the formation of the crystalline shape memory structure requires annealing, all shape memory materials start out as austenite. Before annealing, the materials have amorphous microstructures without order or alignment of crystal lattices. Upon annealing, the highly symmetric B2 crystallization takes place, forming SMA austenite. When it cools, the alloy transforms to martensite for the first time and undergoes self-accommodation. When NiTiCu enters the austenite phase upon reverse transformation, twins are recovered during the transition to B2. As the multiple twin variants transform to the unique B2 variant, the material recovers its original shape. If strain was applied to the martensitic structure causing deformation, the transformation back to B2 includes a macroscopic shape change to its original, annealed shape.

Fabrication of Test Structures

Referring to Figure 2, four-inch diameter 380 μm thick {100} Si wafers (Step 1) with 6000 Å of thermally grown oxide (Step 2) served as substrates for the SMA film deposition. Nickel-titanium-copper films were DC magnetron sputter-deposited at 150 W from a 33 mm diameter alloyed NiTiCu target while heating the substrate (Step 3). Films were deposited in a high vacuum chamber under 5.4×10^{-8} to 1.9×10^{-7} Torr base pressure in 8 mTorr argon. Thermocouples mounted to the surface of the silicon substrate indicated a starting deposition temperature of 510°C and a final deposition temperature of 540°C. Deposition times of 2 hours resulted in average film thickness across the wafer of 1.9 μm with variations of ±0.4 μm. Thickness variation resulted from a low target to substrate diameter ratio, with the thickest film depositing directly in line with the target and diminished film thickness from the center to the edge of the wafer. Film composition, measured by electron microprobe, was 39.5at%Ni, 52at%Ti and 8.5at%Cu.

Patterning of the NiTiCu films was accomplished by photolithography of 1.8 μm thick AZ1518 resist (Step 4) and subsequent wet etching of the alloy in a 20:20:1 hydrochloric acid : nitric acid : hydrofluoric acid ($HCl:HNO_3:HF$) bath (Step 5). During this etch, undercutting of the photoresist removed roughly 5 μm from the edges of the SMA patterns. The oxide layer in this step prevented any silicon from being etched by the combination of HNO_3 and HF.

Window structures were patterned onto the backside of the wafer with a 15 μm AZ4620 photoresist (Step 6) and the wafer was adhered to a handle wafer for deep reactive ion etch (DRIE) processing (Step 7). The exposed oxide was removed with 6:1 buffered HF (Step 8) and the silicon was etched in a ST Systems Advanced Silicon Etch tool (Step 9). Finally, the remaining oxide was reactive ion etched (Step 10) and the wafers were separated in an acetone bath and cleaved (Step 11). A photograph of the resulting test chips is seen in Fig. 3, in which a NiTiCu ribbon with two-2 mm gauge sections is suspended by a silicon frame and electrical contact pads are patterned to allow resistive heating.

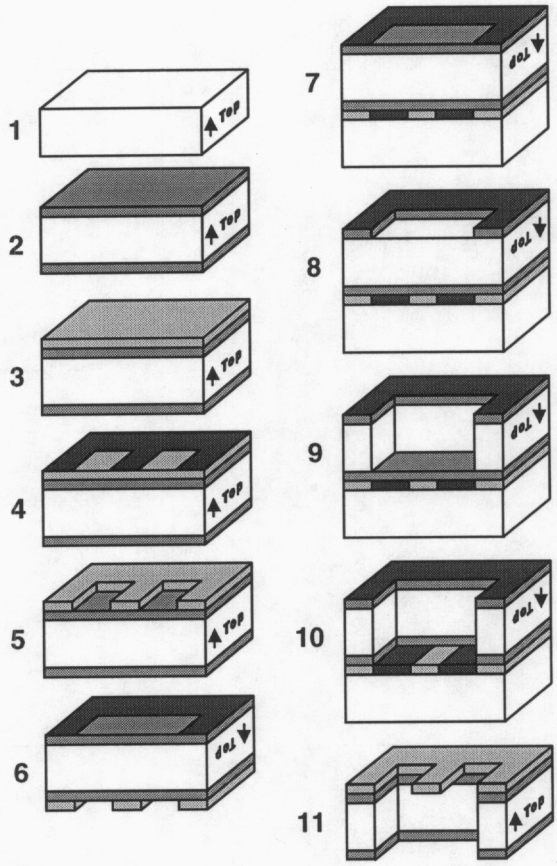

FIG. 2—*Fabrication process for test chips.*

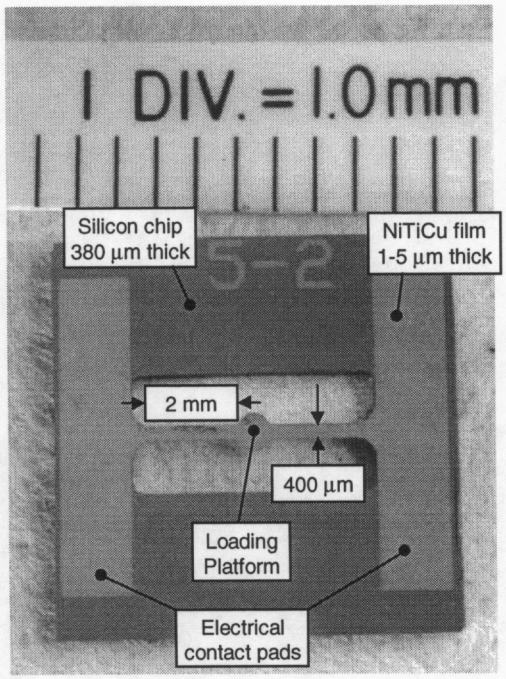

FIG. 3—*Suspended ribbon test chip layout.*

Experimental Method

Unlike traditional mini-tensile testing schemes in which strips of SMA film are totally or partially freed from the substrate and then strained [*19*], the tests described in

this paper utilize out-of-plane stretching without detachment from the substrate. Freestanding fixed-fixed NiTiCu ribbons were patterned on the same wafer as 1 cm square unpatterned (blank) chips used in curvature measurements and test chips with a blank pattern and a window etched beneath in the silicon, forming a NiTiCu membrane for use in pressurized diaphragm measurements.

NiTiCu Ribbon Tensile Test

In an effort to create a non-destructive method for characterizing these films, the out-of-plane test was developed. Rather than sputtering a film and detaching it from its substrate, a film was sputtered and the substrate was etched from under it, leaving a freed ribbon onto which loads and deflections were applied and measured as seen in Fig. 4. This test allows relatively large displacements to be measured and correlated back to small strains. Since film thickness was much less than ribbon width, out-of-plane loading produced negligible bending stresses and the ligaments were assumed to be in a state of uniaxial tension. Depressing the center of the ribbon with a spring-loaded transducer allowed the simultaneous measurement of the load on the ribbon and the consequent deflection of the center.

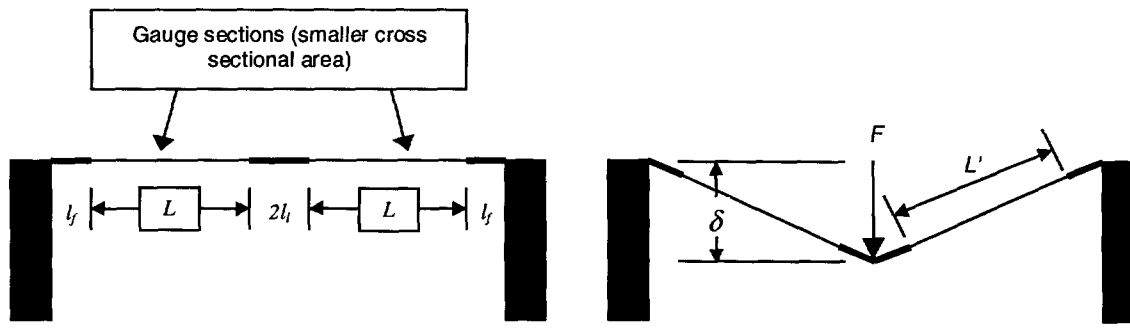

FIG. 4—*Loads and deflections were applied to the ribbons out-of-plane. The resulting force and deflection data yielded stress-strain relationships.*

The stresses in the gauge sections of the ribbon were calculated by resolving the downward force into each of the ribbon legs. In Eq. 1, the true stress along the longitudinal axis of each ribbon leg σ_x is determined by the downward force F, the downward displacement δ, the ribbon length L_o (equal to $L+l_f+l_l$ from above), the original cross-sectional area of the ribbon gauge section $w_o t_o$, the material's Poisson's ratio ν, and the strain in the gauge section $\varepsilon_{g,x}$. Of course, without knowing Poisson's ratio for the material, the engineering stress is merely found by substituting $\nu = 0$.

$$\sigma_x = \frac{F\sqrt{\delta^2 + L_o^2}}{2\delta w_o t_o e^{-2\nu\varepsilon_x}} \tag{1}$$

A first-pass model was used to determine the proportion of strain in the gauge sections and that in the fillets and loading platform. For this model, the assumption was made that since a similar strain (i.e. within the same order of magnitude) exists in the fillet, gauge, and loading platform, a constant elastic modulus would prevail over all three sections. Since each leg of the ribbon is subject to uniaxial tension, the force through the

length is also constant. This allows the assumption of inverse proportionality between strain and cross-sectional area at any given ribbon section. Integrating over the fillet length l_f and the loading platform length l_l for our given geometry produced the relationships between the strain in all three sections: $\varepsilon_{fillet} = 0.651\varepsilon_{gauge}$; $\varepsilon_{load} = 0.510\varepsilon_{gauge}$. These constants of proportionality are denoted C_1 and C_2 respectively for the sake of simplicity. Again using the geometry produced by deflection of the ribbon as seen in Fig. 4, the true strain ε_g is calculated for the gauge section. In Eq. 2, the new variable is the residual strain ε_o on the ribbon, which is subtracted from the measured strain in the equation to yield the actual strain in the ribbon.

$$l_f e^{C_1(\varepsilon_g-\varepsilon_o)} + l_l e^{C_w(\varepsilon_g-\varepsilon_o)} + Le^{(\varepsilon_g-\varepsilon_o)} = \sqrt{\delta^2 + L_o^2} \qquad (2)$$

From this equation, a lookup chart is created to compare the displacement δ to the gauge section strain ε_g, which is necessary for the real-time automated tests performed on these ribbons.

To find the mechanical properties of SMA using the out-of-plane testing concept, the downward displacement and force were measured with a micro-miniature spring-loaded differential variable reluctance transducer (DVRT). The DVRT measured displacements with a resolution of 1 μm, precision of 1.5 μm and full stroke length of 6 mm by differentiating the reluctance output of a magnetic core moving through a coil. When filtered through a demodulator board, the DVRT outputs voltage proportional to its displacement. A calibration lookup table was created to compare this voltage and displacement using an automated linear stage to produce 5 μm incremental motions and measuring the DVRT output voltage. The force calibration of the spring in the DVRT was performed by again making 5 μm incremental motions and measuring the force produced on a load cell against the DVRT output voltage (i.e. the displacement). A lookup chart was made for both calibrations so that maximum accuracy could be obtained during the automated tests.

The force F for Eq. 1 was determined by lookup of the DVRT output voltage, which indicated exactly what the spring compression was and thus the calibrated force. The displacement δ for Eq. 1 and 2 were found by subtracting the lookup value of DVRT compression from the known displacement of the linear stage. Thus, if the stage was advanced 100 μm and the spring had been compressed 50 μm, the total displacement of the center of the ribbon (δ) would be 50 μm.

Bimorph Curvature Test

The test chips with unpatterned film covering a silicon square were subjected to heating and cooling while their radius of curvature ρ was measured to quickly confirm shape memory behavior and measure the residual stress in the unheated film. The biaxial film stress σ_f was calculated by the modified Stoney equation (Eq. 3) [*20*] with a biaxial modulus $E_s/(1-\nu_s)$ equal to 180.5 GPa for {100} silicon [*21*], substrate thickness t_s of 380 μm and film thickness t_f measured by stylus profilometry during the chip fabrication process. This equation provided the data for residual stress at room temperature and the recoverable stress in the film when it was heated to its austenite phase.

$$\sigma_f = \frac{1}{\rho}\frac{E_s t_s^2}{6(1-\nu_s)t_f} \tag{3}$$

Diaphragm Bulge Test

Alloy membranes were pressurized with load P from the backside of test chips with nitrogen. Membrane center deflection δ was measured in the center of the membrane using the DVRT without spring loading. In this case the DVRT provided no counteracting force and could therefore act as a simple displacement sensor. The models used to determine the residual stress σ_o and biaxial Young's modulus $E/(1-\nu)$ of thin films subjected to this test have had various numerical constants [*22-24*] but all follow the same form of Eq. 4, with film thickness t_f and square membrane half-length a.

$$P = C_1 \frac{t_f \delta}{a^2}\sigma_o + C_2(\nu)\frac{t_f \delta^3}{a^4}\frac{E}{1-\nu} \tag{4}$$

In the model we use from Maier-Schneider et. al. [*22*], C_1 has a loose dependence on ν and varies between 3.43 and 3.45 as ν varies from 0 to 0.5, while C_2 is given by Eq. 5.

$$C_2 = 1.994(1-0.271\nu) \tag{5}$$

Although this model is more of an approximation at the high strains seen in the shape memory films (above 2%), it gives an idea of the relationship between the stress and the strain as characterized by other scientists and that seen with the uniaxial tension tests described here. When these equations are coupled with a more general equation to find the strain ε from the center deflection and the half-length as seen in Eq. 6 [*25*], the stress-strain relationship is found by backing out the stress from the calculated Young's modulus and the strain.

$$\varepsilon = 0.462\frac{\delta^2}{a^2} \tag{6}$$

Results

Uniaxial Tensile Tests

Ribbons were loaded and unloaded with the DVRT spring and the forces and displacements were recorded to determine the stress and strain on the ribbons using Eq. 1 and 2. To create an engineering tool, families of stress-strain curves were plotted for various currents through the SMA ribbons. In Fig. 5, one of these families of curves is plotted for a single ribbon. Each curve is labeled with the initial current density through the gauge section. The current was not decreased as strain was added to accommodate for the shrinking cross-sectional area. Therefore, as the tests were performed and the gauge sections were strained the actual current density would rise slightly. This is not shown in the plots in Fig. 5.

The lowest three current densities (12.3, 24.6 and 46.3 A/mm^2) did not heat the ribbon significantly, for the stress-strain behavior was that of martensitic material, with

large deformations taking place to accommodate the stress placed on the ribbon. The highest three current densities (121.3, 145.7 and 169.7 A/mm^2) heated the ribbon enough to cause full reverse transformation and did not allow stress-induced twinning in the material. The intermediate two current densities (97.0 and 73.2 A/mm^2) caused an austenite reverse transformation in the absence of external loads, but progressive loading caused large deformations by stress inducing twins.

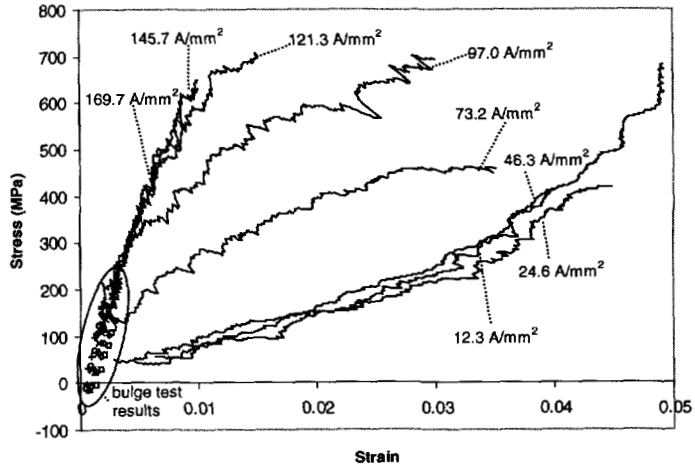

FIG. 5—*Family of stress-strain curves generated for a ribbon during loading at various current densities. The small stress-strain data in the lower left that appear as individual data points were obtained by bulge testing.*

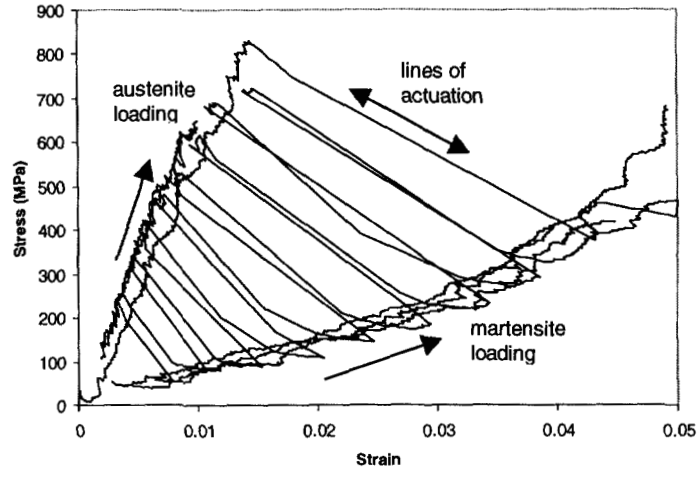

FIG. 6—*Lines of actuation illustrate the recoverable stress and strain achievable by full actuation from martensite to austenite.*

The results shown in Fig. 6 display the behavior of the alloy to a varying current density during loading and unloading of the ribbon in uniaxial tension. In this case, the lower current density, which keeps the alloy fully martensitic, is 0 A/mm^2 and the higher current density, which causes the reverse transformation, is 145.7 A/mm^2. It was later

noticed that the same actuation lines could be produced using the lower current density of 121.3 A/mm^2, because full reverse transformation was still seen. The lines of actuation that connect the martensite and the austenite curves are particular to the loading conditions and therefore are predetermined by the loading geometry and the spring constant of the transducer. It is through actuation lines like this that the stress-strain results can be applied to actuator design and the necessary actuation current density is found.

A microactuator usually employs a biasing force against the SMA recoverable stress to generate bistable motion. In actuator design the alloy is strained at ambient temperature to a certain point on the martensite curve to create a deformation. The equations dictated by the actuator geometry and biasing force determine how much stress and strain the alloy will respond with when heated. In Fig. 6, both a recoverable stress (vertical motion between martensite and austenite plots) and a recoverable strain (horizontal motion between plots) are seen upon actuation. In a design with a constant force on a freed ribbon of NiTiCu, the actuation line would be purely horizontal as the stress remains constant to produce a only a recoverable strain. Vice-versa, if the displacement is held constant, a pure recoverable stress would be produced and the actuation line would be vertical. Knowing the envelope within which the actuator will operate allows the actuator design to be optimized to produce the maximum force and displacement for optimum work output.

The work output per unit volume is simply found by the product of the recoverable stress and the recoverable strain. The longest actuation line in Fig. 6 gives the maximum work output in this test case, in which the ribbon actuates from a stress of 375 MPa and a strain of 0.043 to a stress of 820 MPa and a strain of 0.014. The product of the recoverable stress (445 MPa) and the recoverable strain (0.029) lead to a work output per unit volume of 1.29×10^7 J/m^3. This value is sensible because it lies between those displayed in Fig. 1 for NiTi SMA for a one-time and a fatigue operational regime.

Bimorph Curvature Tests

Curvature results for seven chips from the same substrate are shown in Fig. 7. The residual stress in the martensite phase, equivalent to the martensitic yield stress [*1*], was 95 MPa averaged over all test chips.

A benefit of the curvature test is that transition temperatures for this loading condition can also be discovered. The austenite start temperature, or the point where the reverse transformation begins, is 50°C and the austenite finish temperature is 61°C. The martensite start temperature is encountered upon cooling to 58°C and the martensite finish temperature is 37°C. Note that since this film is part of a bimorph structure rather than a freestanding ribbon, the loading conditions differ and the stress state is likely causing stress-induced twins to form. Twinning results in higher transformation temperatures than those encountered in the freed films as stated by the Clausius-Clapeyron relationship. The relative transformation temperatures and hysteresis width are still useful in design of actuators, for they indicate the suitable ambient temperature in which actuation can occur. For instance, the transformation temperatures indicated here would allow room temperature (23°C) and probably body temperature (37°C) applications, but would not be very useful in automotive applications or hot environments. For these other applications,

different alloys with higher transformation temperatures must be considered and characterized.

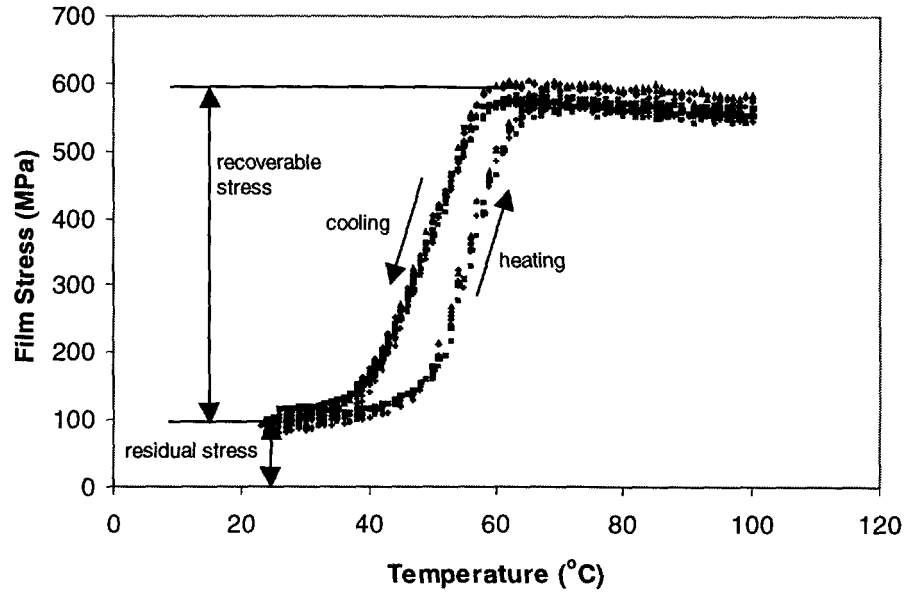

FIG. 7—*Curvature results on seven chips randomly distributed across the processed wafer show uniformity of shape memory effect. Residual stress is determined to be 95 MPa and recoverable stress is ~500 MPa.*

Diaphragm Bulge Tests

Data was taken as the 5mm x 5mm NiTiCu diaphragms were pressurized from the backside at various gauge pressures from 0 to 85 kPa and various current densities from 0 to 25 A/mm^2. The results are seen as individual data points in the bottom left corner (the small stress-strain regime) of Fig. 5. The diaphragms ruptured above 85 kPa, which related to a strain below 0.005 and a stress below 200 MPa. Because only small stresses and strains could be applied to these membranes before catastrophic failure, they were only used to find the low end of the stress-strain curves. These small values were out of the detectable range of the DVRT spring during ribbon deflections due to small amounts of friction in the linear transducer. Using the residual stress value found by the bimorph curvature tests of 95 MPa and solving Eq. 4 with a Poisson's ratio of zero, the engineering stress versus strain were found and the biaxial Young's modulus was ascertained at 80 GPa by averaging the results for each current density.

Conclusions

With the comprehensive testing instrument described here, the design of SMA microactuators is greatly simplified. Accurate material property measurements enable design by the simple determination of the characteristic equations for the device in question and correlation of those equations with the stress-strain curves found by testing ligaments with the same composition and fabrication methods. With the stress-strain curves from these tests, analytic solutions to the design problems associated with SMA

films are ascertained.

The benefits of this instrument do not stop at qualifying films of certain composition to aid in the design of microdevices. It can also be used to qualify the devices after they are fabricated by directly measuring the forces and displacements they achieve while they are loaded. An instrument like this can be used in-line for device qualification, to allow for quality control during a MEMS manufacturing process by checking one or several devices per wafer for forces, deflections, power requirements, and calibration errors all at the same time and in just a few seconds.

Acknowledgements

This work was performed under the auspices of the U.S. Department of Energy by Lawrence Livermore National Laboratory under Contract W-7405-Eng-48.

References

[*1*] Krulevitch, P., Lee, A. P., Ramsey, P. B., Trevino, J. C., Hamilton, J., and Northrup, M. A., "Thin Film Shape Memory Alloy Microactuators," *Journal of Microelectromechanical Systems*, Vol. 5, No. 4, pp. 270-282, December 1996.

[*2*] Miyazaki, S. and Kohl, M., "Recent Development in TiNi-based Shape Memory Alloys," *SPIE Conference on Smart Materials Technologies*, San Diego, California, March 1998, SPIE-Vol. 3324, pp. 2-13.

[*3*] Benard, W. L., Kahn, H., Heuer, A. H., and Huff, M. A., "Thin-Film Shape-Memory Alloy Actuated Micropumps," *Journal of Microelectromechanical Systems*, Vol. 7, No. 2, pp. 245-251, June 1998.

[*4*] Kahn, H., Huff, M. A., and Heuer, A. H., "The TiNi shape-memory alloy and its applications for MEMS," *Journal of Micromechanics and Microengineering*, Vol. 8, pp. 213-221, 1998.

[*5*] Miyazaki, S. and Ishida, A., "Shape Memory Characteristics of Sputter-Deposited Ti-Ni Thin Films," *Materials Transactions, JIM*, Vol. 35, No. 1, pp. 14-19, 1994.

[*6*] Ishida, A., Takei, A., and Miyazaki, S., "Shape memory thin film of Ti-Ni formed by sputtering," *Thin Solid Films*, Vol. 228, pp. 210-214, 1993.

[*7*] Johnson, A. D., "Vacuum-deposited TiNi shape memory film: characterization and applications in microdevices," *Journal of Micromechanics and Microengineering*, Vol. 1, pp. 34-41, 1991.

[*8*] Kennedy, J. B. (translator), *Shape Memory Alloys*, H. Funakubo, Ed., New York: Gordon and Breach, 1984.

[*9*] Perkins, J. and Hodgson, D., "The Two-Way Shape Memory Effect," in *Engineering Aspects of Shape Memory Alloys*, T. W. Duerig, K. N. Melton, D. Stockel and C. M. Wayman, Eds., London, U.K.: Butterworth-Heinemann, pp. 195-206, 1990.

[*10*] Sato, M., Ishida, A., and Miyazaki, S., "Two-Way Shape Memory Effect of Sputter-Deposited Thin Films of Ti 51.3 at.% Ni," *Thin Solid Films*, Vol. 315, pp. 305-309, 1998.

[*11*] Ling, H. C. and Kaplow, R., "Stress-Induced Shape Changes and Shape Memory in the R and Martensite Transformations in Equiatomic NiTi," *Metallurgical Transactions A*, Vol. 12A, pp. 2101-2111, December 1981.

[*12*] Ling, H. C. and Kaplow, R., "Phase Transitions and Shape Memory in NiTi," *Metallurgical Transactions A*, Vol. 11A, pp. 77-83, January 1980.

[*13*] Tietze, H., Müllner, M., Selgert, P., and Assmus, W., "The intermediate phase of the shape-memory alloy NiTi," *Journal of Physics F: Metallurgical Physics*, Vol. 15, pp. 263-271, 1985.

[*14*] Goubaa, K., Masse, M., and Bouquet, G., "Detection of the R-Phase in Ni-Ti

Shape Memory Alloys," *Journal de Physique IV*, Vol. 1, Col. C4, pp. 361-366, November 1991.

[*15*] Bricknell, R. H., Melton, K. N., and Mercier, O., "The Structure of NiTiCu Shape Memory Alloys," *Metallurgical Transactions A*, Vol. 10A, pp. 693-697, June 1979.

[*16*] Krulevitch, P., Ramsey, P. B., Makowiecki, D. M., Lee, A. P., Northrup, M. A., and Johnson, G. C., "Mixed-sputter deposition of Ni-Ti-Cu shape memory films," *Thin Solid Films*, Vol. 274, pp. 101-105, 1996.

[*17*] Bhattacharya, K., "Theory of Martensitic Microstructure and The Shape-Memory Effect," *Shape Memory Alloys: From Microstructure to Macroscopic Properties*, G. Airoldi, I. Müller and S. Miyazaki, Eds., Trans Tech Publications, 1997.

[*18*] Wayman, C. M. and Duerig, T. W., "An Introduction to Martensite and Shape Memory," in *Engineering Aspects of Shape Memory Alloys*, T. W. Duerig, K. N. Melton, D. Stockel and C. M. Wayman, Eds., Boston: Butterworth-Heinemann, 1990.

[*19*] Miyazaki, S., Nomura, K., Ishida, A., and Kajiwara, S., "Recent Developments in Sputter-Deposited Ti-Ni-Base Shape Memory Alloy Thin Films," *Journal de Physique IV*, Vol. 7, Col. C5, pp. 275-280, 1997.

[*20*] Hoffman, R. W., in *Physics of Thin Films*, Vol. 3, G. Hass and T. E. Thun, Eds., New York: Academic, 1996.

[*21*] Brantley, W. A., *Journal of Applied Physics*, Vol. 44, p. 543, 1973.

[22] Maier-Schneider, D., Maibach, J., and Obermeier, E., "A New Analytical Solution for the Load-Deflection of Square Membranes," *Journal of Microelectromechanical Systems*, Vol. 4, No. 4, pp. 238-241, December 1995.

[*23*] Wolf, R. H. and Heuer, A. H., "TiNi (Shape Memory) Films on Silicon for MEMS Applications," *Journal of Microelectromechanical Systems*, Vol. 4, No. 4, pp. 206-212, December 1995.

[*24*] Small, M. K. and Nix, W. D., "Analysis of the accuracy of the bulge test in determining the mechanical properties of thin films," *Journal of Materials Research*, Vol. 7, No. 6, pp. 1553-1563, June 1992.

[*25*] Timoshenko, S., *Theory of Plates and Shells*, New York, NY: McGraw-Hill, pp. 250-307, 1959.